Broadside Scanning Asymmetric SIW LWA With Consistent Gain and Reduced Sidelobe

Ravi Shaw, *Student Member, IEEE*, and Mrinal Kanti Mandal, *Senior Member, IEEE*

***Abstract*— In this paper, a backward-to-forward continuous beam scanning leaky wave antenna is presented in substrate integrated waveguide technology. The antenna radiates from a continuous longitudinal slot etched on its broad wall. The slot is excited by using periodic H-plane steps. An impedance matched unit cell structure is used to suppress the open stopband in the broadside direction. Bloch wave analysis is used to obtain the propagation characteristics of the antenna. However, due to radiation being obtained only from the shunt-type radiating element, namely, the longitudinal slot, a gain dip is observed in the broadside direction. Transversal asymmetry is then introduced in the structure to eliminate the gain dip and obtain the consistent gain. A prototype of the antenna is fabricated and measured. Continuous beam scanning is achieved from -29° to $+30^\circ$ about the broadside direction with a gain variation of less than 2 dB over 8.0–12.4 GHz. A measured peak gain of 16.1 dBi is obtained. Key structural design parameters of the antenna are identified for controlling the leakage rate. Next, Taylor tapered aperture illumination is used to obtain low sidelobe level (SLL). The Taylor tapered antenna is also fabricated with the measured SLL below -21 dB.**

***Index Terms*— Broadside radiation, leaky-wave antenna (LWA), substrate integrated waveguide (SIW), Taylor distribution.**

I. Introduction

LEAKY-WAVE antennas (LWAs) belong to the class of traveling wave antennas that utilizes leakage from a guiding structure to obtain far-field radiation [1]. It has the features of high directivity, simple feeding, and beam scanning with a frequency sweep. Thereby, eliminating the need of additional phase shifters required in traditional phased array antennas. Recent LWAs are utilized in various applications such as the direction of arrival estimation [2], train to wayside communication [3], range-azimuth tracking of humans [4], automotive radars [5], and real-time spectrum analyzers [6].

Over a period, many variants of LWAs are developed based on different wave-guiding structures such as microstrip line [7]–[9], rectangular waveguide [10], dielectric waveguide (NRD) [11], groove guide [12], and substrate integrated waveguide (SIW) [13], [14]. SIW is an alternative to the bulky hollow traditional waveguide. It has the advantages of low profile, low cost, and relatively higher power handling capability compared to popular planar transmission lines. SIW can be easily integrated with other planar circuits [15]. Also, LWAs can be classified based on its geometry leading to uniform, quasi-uniform, and periodic LWAs.

The first known LWA is based on slit-rectangular waveguide introduced by Hansen [16], where the fundamental fast mode is utilized for radiation. The antenna is of a uniform type and exhibits radiation only in the forward quadrant with no broadside radiation. Since then, longitudinal slot LWAs are studied widely primarily for its simplicity in design, fabrication, and the possibility to easily control its radiation pattern [17]–[21].

A conventional periodic LWA achieves backward-to-forward beam scanning. However, it is associated with an open stopband near the broadside direction leading to severe gain degradation [22]. Periodic LWAs in [23]–[25] have either a gain dip or no radiation at all in the broadside direction.

Various techniques are proposed to solve the open stopband problem. In [26], a backward-to-forward scanning LWA based on CRLH-TL is proposed. The structure is quasi-periodic and radiation is obtained from the zeroth-order harmonic. In [27], a collinear-slotted periodic LWA based on double-ridged SIW is presented. Although the open stopband is suppressed, two layers and double ridge increase the fabrication cost and complexity. In [28], a series–shunt radiating unit cell is proposed for suppressing the open stopband. However, a gain dip in the broadside direction is still present. Similar broadside gain dip is observed in [29]–[34].

Recently, the problem of gain equalization through broadside is studied based on LWAs with longitudinal [35] and transversal asymmetries [36]. Longitudinal asymmetry in the unit cell of a periodic LWA affects only its shunt radiating element. Increasing longitudinal asymmetry increases radiation from the shunt radiating element. Whereas transversal asymmetry helps to achieve radiation efficiency equalization through the broadside direction even for a single type of radiating element, namely, either a series or shunt-type element. Thus, a combination of both longitudinal and transversal asymmetry provides more degree of freedom in antenna design [37].

In this paper, a broadside radiating SIW LWA is designed. Both longitudinal and transversal asymmetries are used. A longitudinal slot on the broad wall acts as a shunt radiator. Longitudinal asymmetry in the form of H-plane steps excites the longitudinal slot. A unit-cell-based analysis is followed to obtain good input impedance matching through the broadside direction. However, reduced radiation efficiency is observed in the broadside direction due to radiation being obtained only from shunt-type radiating element, namely, the

Manuscript received January 18, 2018; revised October 30, 2018; accepted November 6, 2018. Date of publication November 21, 2018; date of current version February 5, 2019. *(Corresponding author: Mrinal Kanti Mandal.)*

The authors are with the Department of Electronics and Electrical Communication Engineering, IIT Kharagpur, Kharagpur 721302, India (e-mail: ravishaw@iitkgp.ac.in; mkmandal@ieee.org).

Color versions of one or more of the figures in this paper are available online at http://ieeexplore.ieee.org.

Digital Object Identifier 10.1109/TAP.2018.2882685

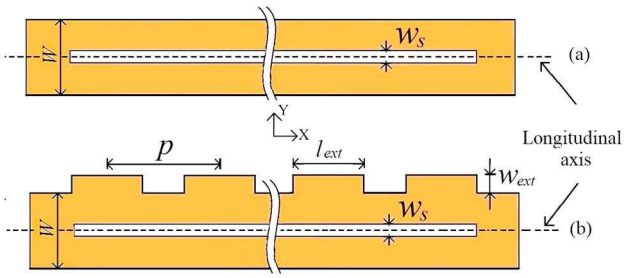

Fig. 1. Top view of SIW structure with (a) longitudinal slot placed symmetrically and (b) same structure after addition of H-plane steps on one side.

longitudinal slot. Next, transversal asymmetry is introduced for equalizing gain through broadside direction. Also, Taylor distribution is applied to obtain reduced sidelobe level (SLL) by simultaneously tapering the widths of the slot and H-plane step to obtain the desired leakage profile. Both the nontapered and tapered antennas are fabricated and measured showing good agreement with the simulated results.

II. LWA With Single-Side H-Plane Steps

Fig. 1(a) shows the top view of an SIW structure with a longitudinal slot placed centrally on the broad wall. The structure is symmetric with respect to the longitudinal axis leading to no excitation of the slot. Fig. 1(b) shows the same structure after the addition of periodic H-plane steps on one side. H-plane step makes the structure longitudinally asymmetric and helps to excite the longitudinal slot. The addition of periodicity to the structure causes an infinite number of space harmonics (Floquet modes) to be generated [1]. The phase constant of the nth space harmonic β_n satisfies

$$\beta_n p = \beta_0 p + 2n\pi \tag{1}$$

where p is the periodicity, n is the harmonic order, and β_0 is the phase constant of the fundamental ($n = 0$) space harmonic. Another simple relationship exists between the main-beam direction θ measured from the broadside direction and the phase constant of an LWA given by

$$\sin\theta \approx \frac{\beta_n}{k_0}. \tag{2}$$

For a single-beam operation, β_{-1}, i.e., the first spatial harmonic is the desired mode of radiation. For the $n = -1$st space harmonic, from (1) and (2)

$$\sin\theta \approx \frac{\beta_{-1}}{k_0} = \frac{\lambda_0}{\lambda_{g0}} - \frac{\lambda_0}{p}, \tag{3}$$

where λ_{g0} is the guided wavelength of the fundamental mode in SIW. Thus, to obtain broadside ($\theta = 0°$) radiation at f_b, the periodicity p should be chosen using (3) as

$$p \approx \lambda_{g0} \text{ at } f_b. \tag{4}$$

The width W of the hosting SIW is chosen satisfying the relation [1]

$$W > \frac{\pi}{k_{c,slow}\sqrt{\varepsilon_r - 1}} \tag{5}$$

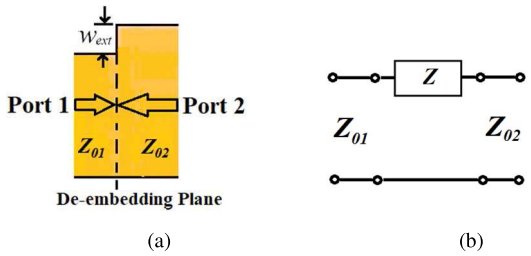

Fig. 2. (a) H step junction without the slot and (b) its equivalent network.

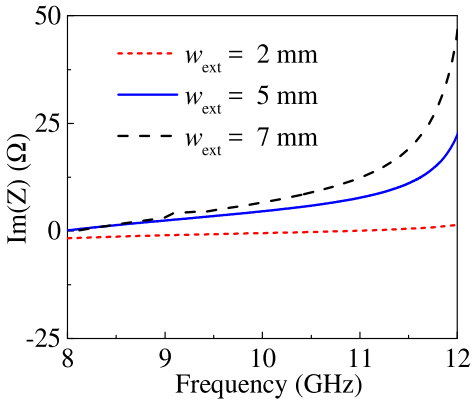

Fig. 3. Plot of the imaginary part of Z for different w_{ext} values.

where ε_r is the relative dielectric constant, $k_{c,slow}$ is the free space wavenumber at the desired slow wave cutoff frequency $f_{c,slow}$,i.e., the frequency from which the slow-wave region starts. A 1.58 mm thick 3M substrate with relative dielectric constant $\varepsilon_r = 2.5$ and loss tangent $\tan\delta = 0.0019$ is considered for all full-wave simulations using CST Microwave Studio.

The periodicity p and the width W are 27 and 16.9 mm, respectively, satisfying (4) and (5) for $f_b = 9.5$ GHz. To suppress the open stopband problem at broadside, an impedance matched unit cell is considered. Fig. 2(a) shows an H-plane step junction without the slot. The equivalent network model is shown in Fig. 2(b), where Z_{01} and Z_{02} are the characteristic impedances for the TE_{10} mode of the respective waveguides [38]. Effect of the step junction is represented by the series element Z. The generalized S matrix for this network is [39]

$$\frac{1}{D_s}\begin{pmatrix} Z + Z_{02} - Z_{01} & 2\sqrt{Z_{01}Z_{02}} \\ 2\sqrt{Z_{01}Z_{02}} & Z + Z_{01} - Z_{02} \end{pmatrix} \tag{6}$$

where $D_s = Z + Z_{01} + Z_{02}$. Full wave simulation is used to extract the Z values for different w_{ext} using (6) and is shown in Fig. 3. It is observed that Z is capacitive for smaller w_{ext} but becomes inductive with increasing w_{ext}. Whereas, a longitudinal slot on the broad wall used for radiation provides a shunt capacitive loading. This series inductive and shunt capacitive pair is used to suppress the open stopband problem at broadside [28].

A unit cell of the structure with the slot is shown in Fig. 4(a). The slot is shown shifted from the longitudinal axis by s for proper excitation and input matching. The $|S|$-parameters of the unit cell without slot is shown in Fig. 4(b) with

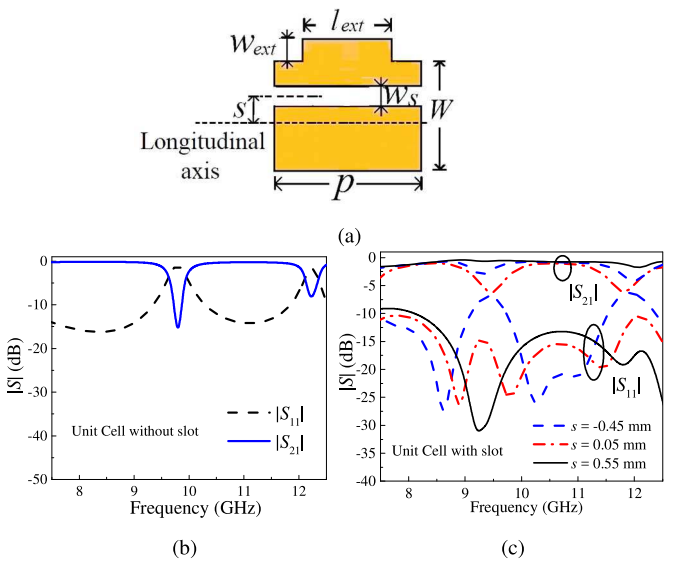

Fig. 4. (a) Top view of a unit cell of the longitudinally asymmetric SIW structure. $|S|$ parameters for the unit cell (b) without slot and (c) with a slot having different slot offsets.

$w_{ext} = 5$ mm and $l_{ext} = 17$ mm. It shows the presence of a stop band. The $|S|$-parameters of the same unit cell with a slot width of 4 mm and different slot shifts are shown in Fig. 4(c). It is observed that the proper slot shift can suppress the stopband, leading to good impedance matching of the unit cell. The Bloch wave analysis is used to obtain the propagation characteristics of the LWA. The propagation constant is obtained using the infinite periodic structure formulation [39]

$$\gamma = \alpha + j\beta = \frac{1}{p}\cosh^{-1}\left(\frac{A+D}{2}\right) \tag{7}$$

where γ is the complex propagation constant, α is the attenuation constant, β is the phase constant, p is the periodicity, and A and D are the transmission parameters of the single unit cell. The slot width w_s, slot offset s, H-plane step length l_{ext}, and H-plane step width w_{ext} of the unit cell are varied to optimize the Bloch impedance to obtain good impedance matching in the broadside direction at f_b. The optimized dimensions are $w_{ext} = 5$ mm, $l_{ext} = 17$ mm, $s = 0.55$ mm, and $w_s = 4.5$ mm. Normalized Bloch impedance of the optimized unit cell is shown in Fig. 5(a). It is observed that the imaginary part of the normalized Bloch impedance is close to zero over 8–12 GHz so that minimal reactive power is reflected back. The corresponding dispersion curve using the optimized unit cell is shown in Fig. 5(b). The broadside radiation is predicted to be at 9.45 GHz. A plot of the E-field in the transverse yz plane in Fig. 6 shows slot excitation at the broadside frequency of 9.45 GHz.

An LWA is designed by cascading 12 unit cells. At both the sides, 50 Ω microstrip to SIW transitions is used [40]. The length of the slot is 297 mm and the total length of the antenna including the transitions is 365 mm. The simulated $|S|$-parameters of the LWA with the second port matched terminated with a 50 Ω load is shown in Fig. 7. The $|S_{11}|$ of the antenna is below −10 dB over 7.6–12.5 GHz.

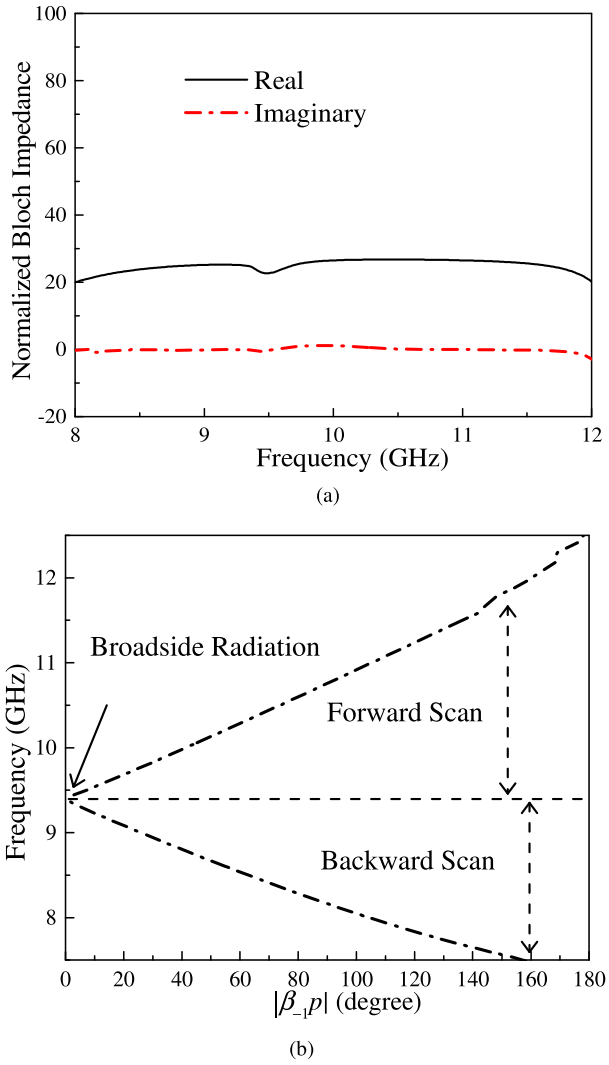

Fig. 5. (a) Bloch Impedance normalized with respect to 50 Ω and (b) dispersion curve using the unit cell of Fig. 4(a).

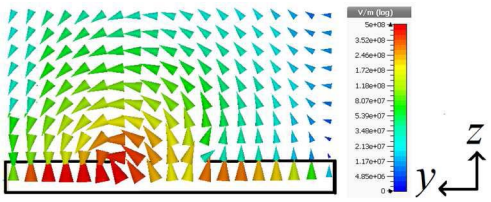

Fig. 6. E-field in the yz plane at $f_b = 9.45$ GHz.

The corresponding $|S_{21}|$ plot of the antenna shows that considerable power reaches at the terminating matched load, thus providing a scope to increase leakage from the antenna.

Simulated antenna radiation patterns at three different frequencies in the zx-plane are shown in Fig. 8. It is evident from the gain plot in Fig. 9 that the gain at $f_b = 9.45$ GHz shows a dip even with good impedance matching. The corresponding radiation efficiency plot of the antenna in Fig. 10 shows a similar dip at f_b. This dip is attributed to the fact that the radiation obtained here is only from a single type of radiating element, i.e., the longitudinal slot behaving as a

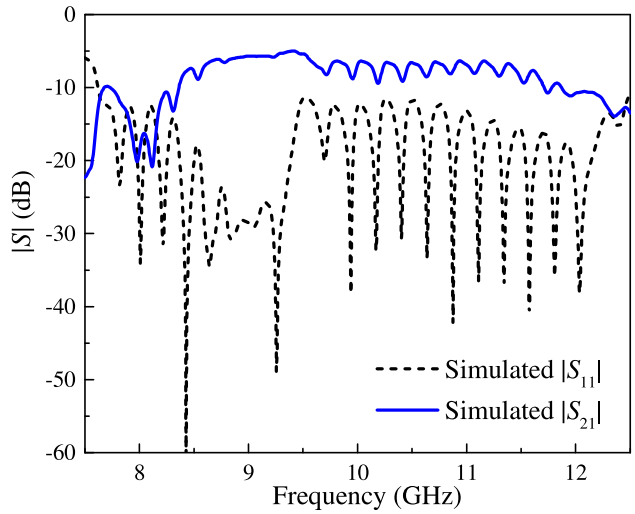

Fig. 7. $|S|$-parameters of the SIW LWA with H-plane step on one side.

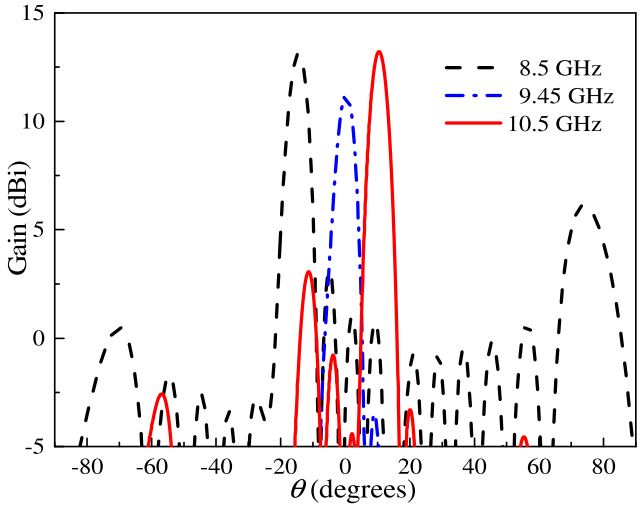

Fig. 8. Simulated radiation pattern of SIW LWA with H-plane steps on one side.

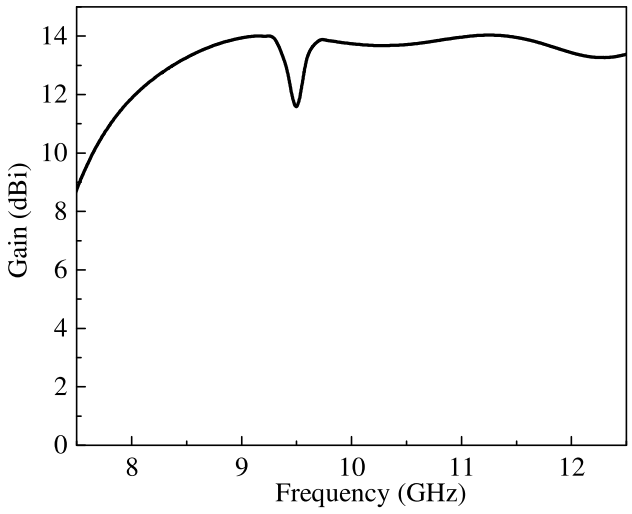

Fig. 9. Simulated gain versus frequency plot of the SIW LWA with H-plane step on one side.

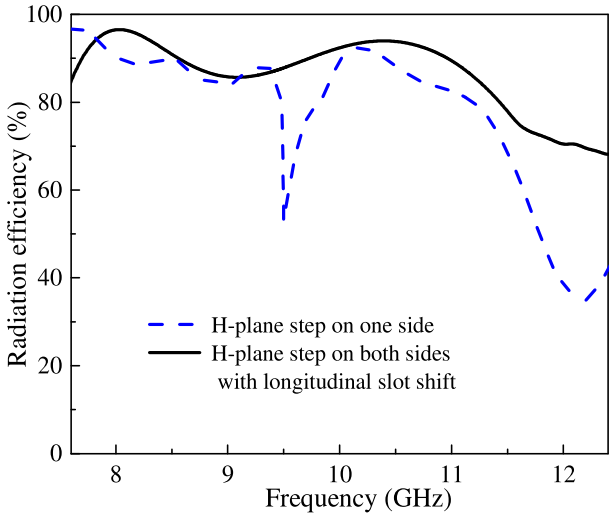

Fig. 10. Simulated radiation efficiency plot for two designs of the antenna.

shunt-type radiating element. In Section III, the antenna design is modified to equalize the broadside gain using Q balancing.

III. LWA With H-Plane Step on Both Sides

Fig. 11 shows the modified configuration where H-plane steps are used on both sides, which increases the leakage α. The H-plane steps on both sides have the same period p, width w_{ext}, and length l_{ext}. The corresponding unit cell without the slot is shown in Fig. 12. The unit cell is divided into different regions. The transmission matrix of the unit cell is obtained by multiplying individual block matrices maintaining the same order as in the unit cell. The waveguide sections in the regions 1, 3, and 5 are identical except the difference in lengths. Here, $l_1 = l_5 \neq l_3$.

Thus, for the TE_{10} mode of the waveguide, the propagation constant $\beta_1 = \beta_3 = \beta_5$ and the characteristic impedance $Z_{01} = Z_{03} = Z_{05}$. The regions 2 and 4 with $l_2 = l_4 = \Delta l$ is modeled by symmetric π network, as shown in Fig. 13. The equivalent network model of the modified unit cell without the

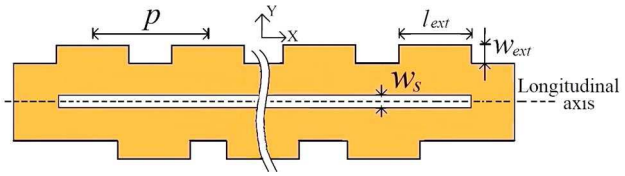

Fig. 11. Modified structure with H-plane steps on both sides to increase leakage.

slot is shown in Fig. 14. The transmission matrices of different sections are

$$[ABCD]_n = \begin{bmatrix} \cos(\beta_n l_n) & jZ_{0n}\sin(\beta_n l_n) \\ jY_{0n}\sin(\beta_n l_n) & \cos(\beta_n l_n) \end{bmatrix} \quad (8)$$

where $n = 1$, 3, and 5. Also, $[ABCD]_1 = [ABCD]_5$ since $l_1 = l_5$. The transmission matrix for the π-network for either Sections II or IV is

$$[ABCD]_{2,4} = \begin{bmatrix} 1 + Z/Z' & Z \\ (2 + Z/Z')/Z' & 1 + Z/Z' \end{bmatrix}. \quad (9)$$

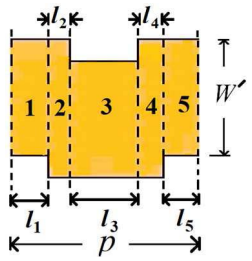

Fig. 12. Schematic of the modified unit cell without slot.

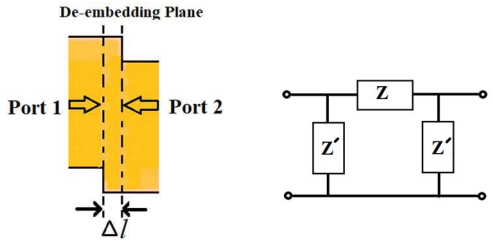

Fig. 13. (a) Schematic of the region 2 or 4 of the modified unit cell and (b) corresponding π-network model.

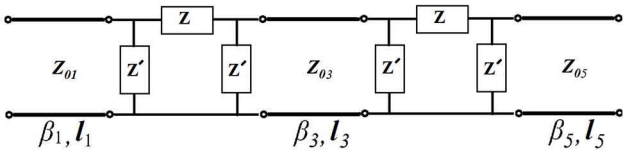

Fig. 14. Equivalent network model of the modified unit cell.

Then, the overall transmission matrix is

$$\begin{bmatrix} A'D' + B'C' & 2A'B' \\ 2C'D' & A'D' + B'C' \end{bmatrix}$$

where

$$A' = \begin{pmatrix} A_2\cos(\beta_1(l_1+l_0)) + jZ_{01}C_2\sin(\beta_1 l_1)\cos(\beta_1 l_0) \\ +jY_{01}B_2\cos(\beta_1 l_1)\sin(\beta_1 l_0) \end{pmatrix}$$

$$B' = \begin{pmatrix} jZ_{01}A_2\sin(\beta_1(l_1+l_0)) - Z_{01}^2C_2\sin(\beta_1 l_1)\sin(\beta_1 l_0) \\ +B_2\cos(\beta_1 l_1)\cos(\beta_1 l_0) \end{pmatrix}$$

$$C' = \begin{pmatrix} jY_{01}A_2\sin(\beta_1(l_1+l_0)) - Y_{01}^2B_2\sin(\beta_1 l_1)\sin(\beta_1 l_0) \\ +C_2\cos(\beta_1 l_1)\cos(\beta_1 l_0) \end{pmatrix}$$

$$D' = \begin{pmatrix} A_2\cos(\beta_1(l_1+l_0)) + jZ_{01}C_2\cos(\beta_1 l_1)\sin(\beta_1 l_0) \\ +jY_{01}B_2\sin(\beta_1 l_1)\cos(\beta_1 l_0) \end{pmatrix}$$

where $l_3 = 2l_0$. Now, from [39],

$$S_{11} = \frac{A + B/Z_{01} - CZ_{01} - D}{A + B/Z_{01} + CZ_{01} + D}. \tag{10}$$

Then, the condition for matching putting $S_{11} = 0$ is

$$\begin{aligned} \mathrm{Re}[Z] &= \mathrm{Re}[Z']\left(Z_{01}^2\left(\frac{1}{X} + \frac{1}{Y}\right)\right) \\ \mathrm{Im}[Z] &= -\mathrm{Im}[Z']\left(Z_{01}^2\left(\frac{1}{X} + \frac{1}{Y}\right)\right) \end{aligned} \tag{11}$$

where $X = (\mathrm{Re}[Z'] - Z_{01})^2 + (\mathrm{Im}[Z'])^2$ and $Y = (\mathrm{Re}[Z'] + Z_{01})^2 + (\mathrm{Im}[Z'])^2$.

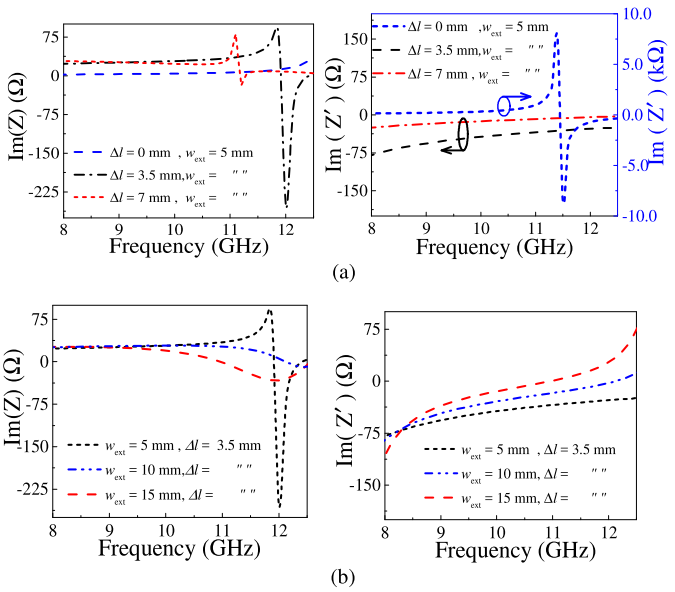

Fig. 15. Extracted values of Z and Z' from a full-wave simulation of the common region in Fig. 13 for (a) different Δl with w_{ext} fixed and (b) different w_{ext} with Δl fixed.

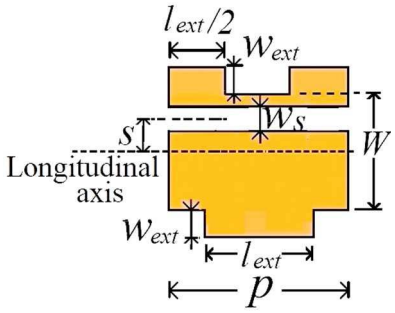

Fig. 16. Unit cell of the modified LWA structure shown in Fig. 11.

From (11), it follows that the unit cell can be matched when Z is inductive and Z' is capacitive or vice versa over the desired frequency band. Since the longitudinal slot has a shunt capacitive effect, which adds to the shunt element Z', it is mostly capacitive. The Z and Z' values are extracted from full-wave simulation and their imaginary parts are plotted for different values of Δl and w_{ext}. Fig. 15(a) shows that for a fixed w_{ext} and with increasing Δl, the Z' value becomes capacitive while the inductive regime of Z decreases to a narrower frequency range. This limits the range for Δl value variation for good matching over an intended frequency range. Similarly, from the plot in Fig. 15(b), a range for variation of w_{ext} is also found with Δl fixed. These plots are used as a guideline for choosing appropriate values of w_{ext} and Δl to keep Z and Z' in the inductive and capacitive regime, respectively.

The unit cell is loaded with a longitudinal slot as shown in Fig. 16 and Bloch impedance is optimized to obtain good impedance matching by varying w_{ext}, Δl, w_{s}, and s. The optimized unit cell dimensions are $W = 16.9$ mm, $p = 27$ mm, $s = 0$ mm, $w_s = 6.45$ mm, $l_{ext} = 17$ mm, and

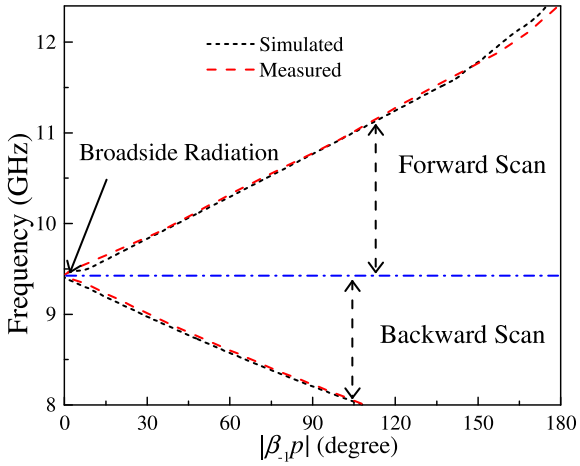

Fig. 17. Simulated and measured propagation constant for the antenna with both side H-step.

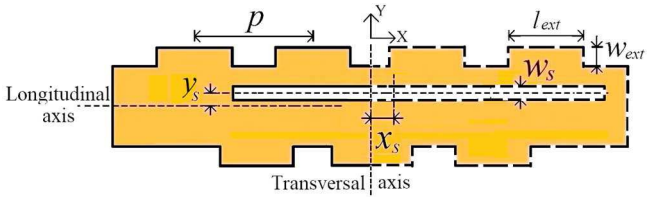

Fig. 18. Top view of the LWA showing the slot shift x_s and y_s along x- and y-axes, respectively. Thick solid line: left part of the antenna. Thick dotted line: right part of the antenna.

$w_{ext} = 5$ mm. Fig. 17 shows the simulated and measured propagation constant of the antenna showing broadside radiation at 9.45 GHz. A close match is observed between the measured and simulated results. Using the relation

$$e_r = 1 - e^{-2\alpha L} \tag{12}$$

where e_r is the radiation efficiency, α is the leakage constant, and L is the slot length, the required antenna length is determined to radiate at least 90% of the input power [1]. The LWA is designed by cascading 13 unit cells with slot length $L = 319$ mm and slot width $w_s = 6.45$ mm.

Since the unit cells are transversally symmetric, the antenna obtained after cascading the unit cells still shows a broadside gain dip. To equalize the gain through the broadside, the structure is made transversally asymmetric. The radiation characteristics of the antenna are studied by finding the antenna Q factor. By making the dielectric and metal losses zero in full wave simulator, Q factor due to only radiation is found using [36]

$$Q = \omega \frac{\partial\beta/\partial\omega}{2\alpha}. \tag{13}$$

Fig. 18 shows the antenna schematic with the longitudinal slot shifted by y_s and x_s with respect to the longitudinal and transversal axis, respectively. The Q factor of the antenna calculated using (13) for different y_s keeping x_s fixed at 0 mm is shown in Fig. 19. It shows Q factor peaking at the respective broadside frequencies for both positive and negative y_s shift. No improvement in Q value equalization is observed near broadside since the structure remains transversally symmetric on giving a y_s shift.

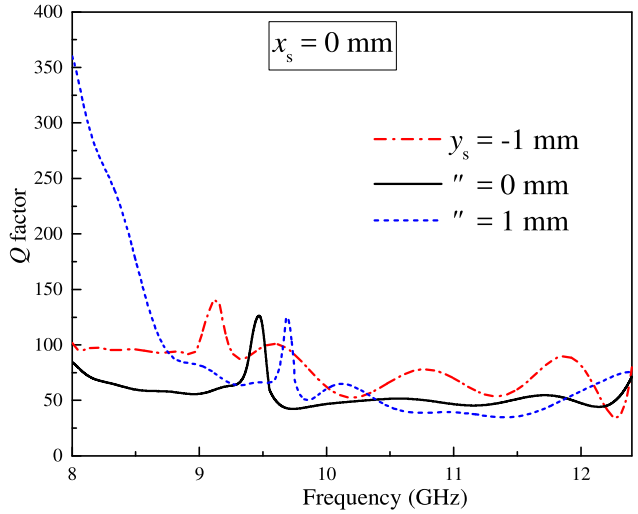

Fig. 19. Antenna Q factor for different slot shifts of y_s with $x_s = 0$.

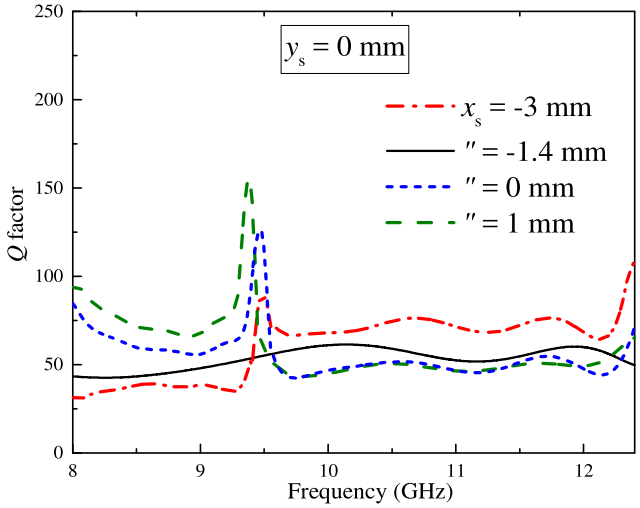

Fig. 20. Antenna Q factor for different slot shifts of x_s with $y_s = 0$.

Fig. 20 shows the antenna Q-factor plot for different x_s values keeping y_s fixed at 0 mm. For increasing positive values of x_s, the Q at broadside increases resulting in overall large variation in Q. Whereas, for a negative x_s, the overall variation of Q decreases and is minimum for $x_s = -1.4$ mm. However, for further negative x_s, the overall Q variation starts to increase again. Thus, the Q balancing condition is achieved for $x_s = -1.4$ mm resulting in gain equalization at broadside frequency.

A parametric study of this transversal shift x_s versus the antenna gain at $f_b = 9.45$ GHz is shown in Fig. 21. As predicted from the Q value plots, it is observed that positive x_s shift (right side) increases the broadside gain dip. A negative shift increases leakage from the slot tending toward broadside gain equalization. The optimum value of x_s is -1.4 mm. Fig. 22 shows α plots for both the antennas [41]. It is observed that leakage is higher and increases when H-steps are used on both the sides with slot shift.

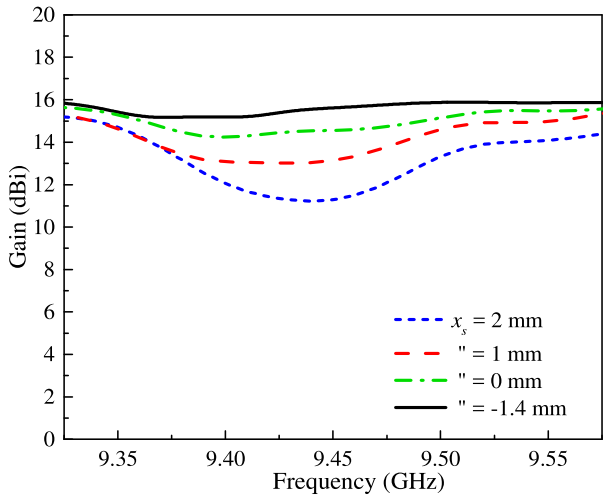

Fig. 21. Gain variation near broadside direction with the slot shift x_s variation.

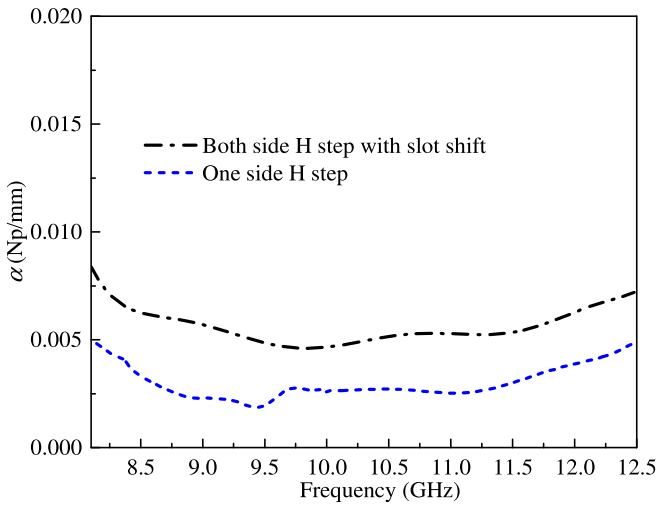

Fig. 22. Leakage α plot comparison for two antenna structures.

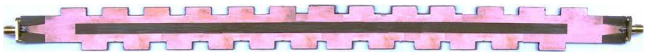

Fig. 23. Photograph of the fabricated LWA with both side H-plane steps and slot shift.

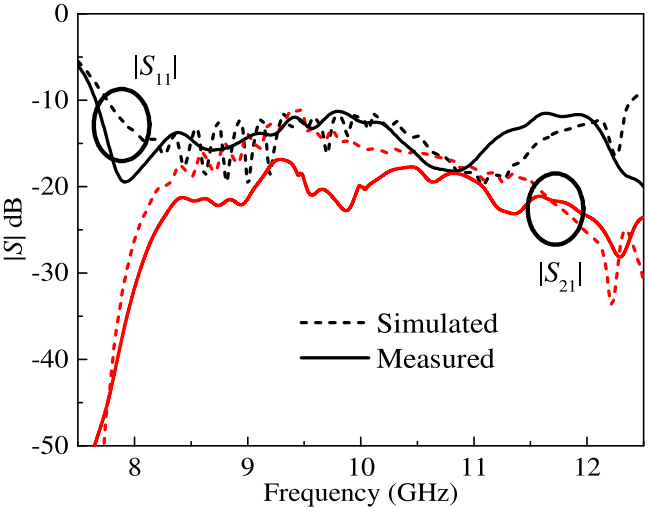

Fig. 24. $|S|$-parameters of the SIW LWA in Fig. 23.

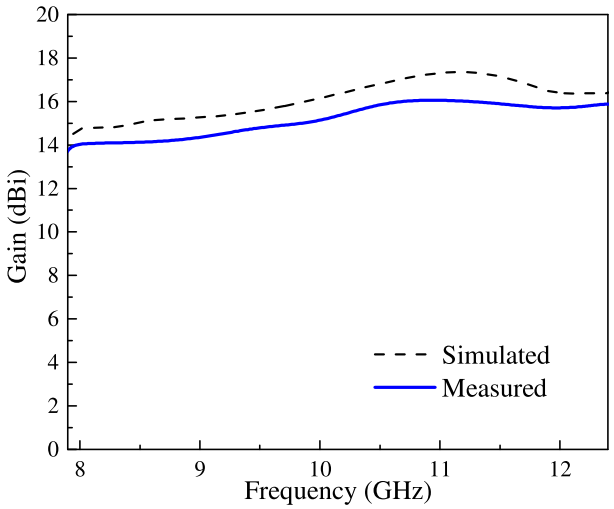

Fig. 25. Gain plot of the SIW LWA in Fig. 23.

A. Antenna Design Steps

The design steps for the antenna are summarized as follows.

1) SIW width is first calculated from (5).
2) The periodicity p for H-plane step is calculated at the desired f_b from (4).
3) The allowed range for w_{ext} and Δl are found by a parametric sweep, as shown in Fig. 15.
4) The Bloch impedance of the unit cell with the longitudinal slot is optimized by varying w_{ext}, Δl, w_s, and s for good impedance match.
5) The number of unit cells is found using (12) for at least 90% radiation.
6) The broadside Q factor and, hence, the broadside gain are equalized using (13) by shifting the longitudinal slot resulting in transversal asymmetry.

A photograph of the fabricated antenna using the same 3M substrate is shown in Fig. 23. The sidewalls are realized using in-house copper deposition process. The simulated and measured $|S|$-parameters of the antenna are shown in Fig. 24. Measured $|S_{11}|$ is below -10 dB over 7.6–12.5 GHz.

The simulated and measured antenna gains in Fig. 25 shows that the gain dip present earlier at $f_b = 9.45$ GHz is now absent. It is also observed that the antenna gain is consistent with the measured gain variation of less than 2 dB over 8–12.4 GHz. The plot in Fig. 10 also shows the corresponding improvement in the radiation efficiency at broadside. The main beam of the antenna scans from $-29°$ in the backward direction at 8 GHz to $+30°$ in the forward direction at 12.4 GHz. It may be noted that the radiating magnetic current direction of the longitudinal slot is parallel to the antenna axis. Therefore, the main lobe scanning from backward to end-fire direction could not be achieved since the axis-directed

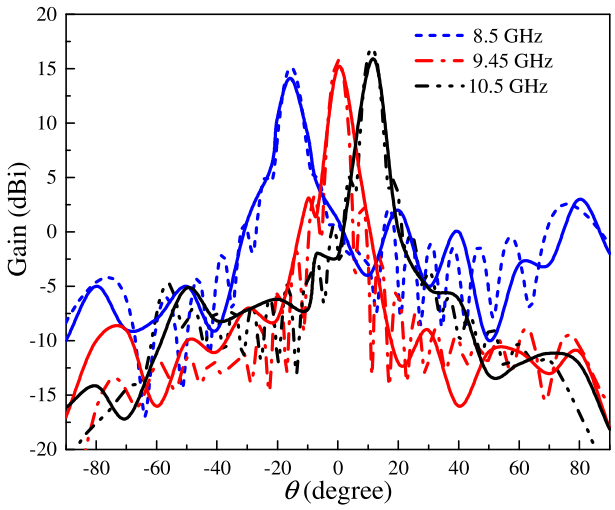

Fig. 26. Measured (solid line) and simulated (dashed line) gain plots at different frequencies.

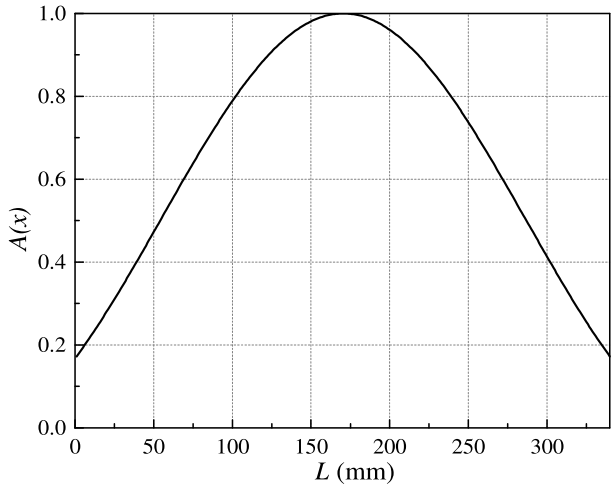

Fig. 27. Diagram showing the aperture illumination $A(x)$ variation with slot length L using -25 dB SLL Taylor distribution.

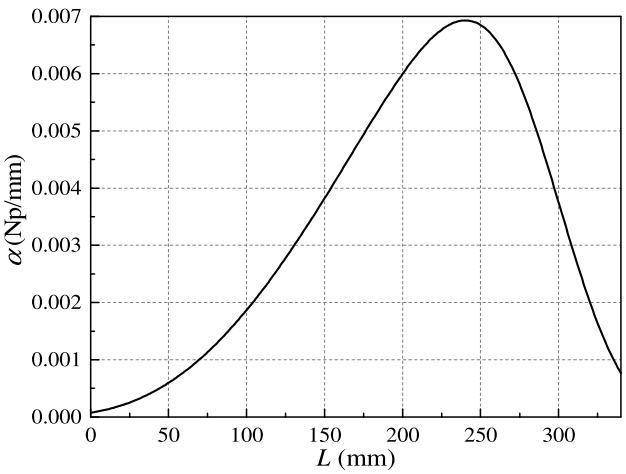

Fig. 28. Leakage constant α variation along the slot length using -25 dB SLL Taylor distribution.

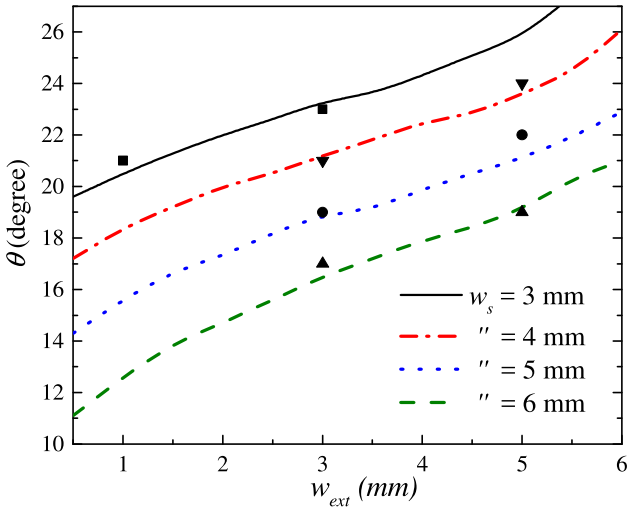

Fig. 29. Main-beam angle variation with w_{ext} for different values of slot width w_s at 11 GHz. Symbols: measured values.

current element patterns have nulls in the axis direction [42]. Fig. 26 shows the measured radiation patterns in the zx plane at 8.5, 9.45, and 10.5 GHz with the measured SLL of -10 dB, -11.5 dB, and -12.5 dB, respectively. In Section IV, the SLL of the antenna is reduced further using Taylor tapering.

IV. Taylor Tapered LWA

The slot aperture illumination $A(x)$ is tapered using a -25 dB SLL Taylor distribution, as shown in Fig. 27. The corresponding leakage $\alpha(x)$ variation along the slot length is [1]

$$\alpha(x) = \frac{\frac{1}{2}|A(x)|^2}{\frac{1}{1-R}\int_0^L |A(x)|^2 dx - \int_0^x |A(x)|^2 dx} \tag{14}$$

where the terminating end of the antenna is designed to absorb a fraction R of the input power. Here, R is taken as 10%, such that 90% of the input power is radiated at 11 GHz. Taking $L = 340$ mm and using the amplitude distribution $A(x)$ as in Fig. 25, the leakage constant profile along the slot length is obtained using (14) and is shown in Fig. 28.

Variation of the slot width w_s changes the leakage constant α, but at the same time, it also affects β of the antenna due to change in its geometry. However, β of the antenna should be kept fixed so that at a given frequency different parts of the antenna radiate in the same direction. This is accomplished here by varying w_{ext} along with w_{s}. The full-wave simulator is used to obtain the variation of the main-beam angle θ and leakage constant α with w_s and w_{ext} at 11 GHz.

A. Main-Beam Angle Variation

Fig. 29 shows simulated θ variation with w_{ext} for different values of w_s. Eight antenna structures are fabricated for verification. The measured results are shown in symbols. It is observed that the main-beam angle increases with increasing w_{ext} when w_s is kept fixed, whereas, for a fixed w_{ext}, the main-beam angle increases with decreasing w_s.

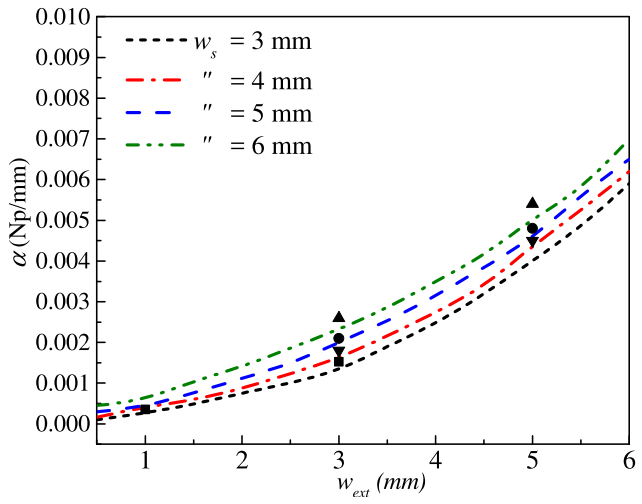

Fig. 30. Leakage constant α variation with w_{ext} for different values of slot width w_s at 11 GHz. Symbols: measured values.

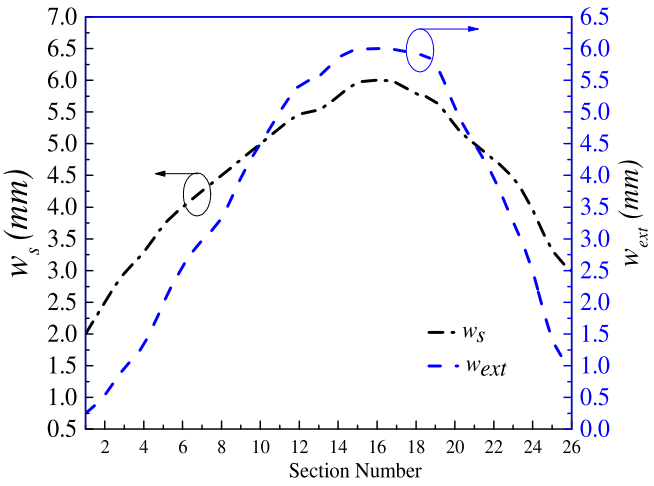

Fig. 31. Design curve of Taylor LWA for the main beam at $\theta = 20°$ at 11 GHz.

B. Leakage Constant Variation

Fig. 30 shows α variation with w_{ext} for different w_s. The measured results for the fabricated antennas are shown in symbols. The leakage constant α increases with increasing w_s when w_{ext} is kept fixed. Also, for a fixed w_s, α increases with increasing w_{ext}.

C. Fabrication and Measurement

To implement the Taylor tapering profile, slot length L is divided into 26 equal sections with each section measuring nearly 13 mm. Using the parametric studies in Figs. 29 and 30, w_s and w_{ext} are chosen for each section keeping the main beam fixed at $\theta = 20°$ at 11 GHz. The corresponding design curves are shown in Fig. 31. A prototype of the Taylor tapered LWA is fabricated using the same 3M substrate. A photograph of the fabricated antenna is shown in Fig. 32. The simulated and measured $|S|$-parameters of the antenna are shown in Fig. 33. The simulated and measured radiation patterns in the zx plane at 8.5, 9.2, 10, and 11 GHz are shown in Fig. 34.

Fig. 32. Photograph of the Taylor tapered LWA.

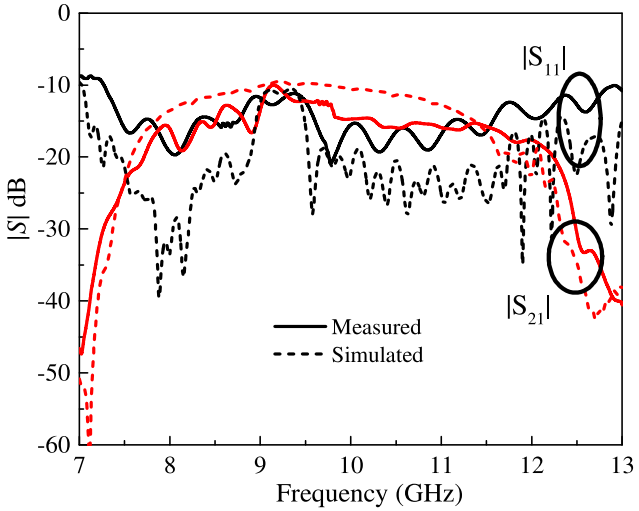

Fig. 33. Simulated and measured $|S|$-parameters of the Taylor tapered LWA.

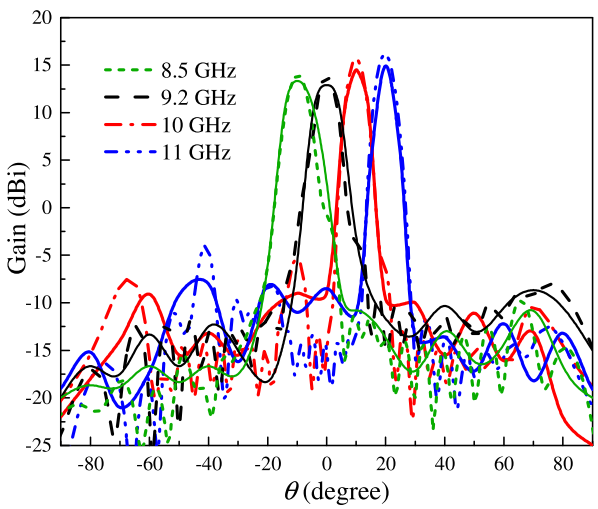

Fig. 34. Simulated (dashed line) and measured (solid line) radiation patterns of the Taylor tapered LWA.

The measured SLLs are below −22 dB, −21 dB, −21.5 dB, and −22.5 dB, respectively.

Table I compares the present antenna with other recent LWAs. The designs in both [23] and [25] show broadside gain dip. The antenna in [27] shows no gain dip at broadside but uses double-ridged dual-layer SIW, leading to fabrication complexity, higher cost, and difficulty in integration. All the LWAs in [28]–[33] show a broadside gain dip with a maximum gain variation of more than 3 dB. The dual-layer antenna design in [34] suffers from broadside gain dip and a large gain variation of 16 dB. In contrast, the present antenna provides a maximum gain variation of 2 dB. Also, use of a single-layer printed circuit board without any ground plane

TABLE I
COMPARISON WITH OTHER LWAS

Type	Freq. (GHz)	Broad-side gain dip	Max gain variation (dB)	Peak gain (dBi)	Length @ f_b
[23] SIW	28–34	Yes	–	–	–
[25] Dual layer ridged SIW	8–20	Yes	–	–	–
[27] Double ridged dual layer SIW	8–12	No	< 2	12.5	$\approx 11\ \lambda_0$
[28] SIW	9–14	Yes	< 4	12	$\approx 7.9\ \lambda_0$
[29] Multilayered SIW	8–13	Yes	< 5	12.8	$\approx 4.5\ \lambda_0$
[30] Parallel Plate Wave-guide	2.35–5.45	Yes	< 5	–	–
[31] SIW and HMSIW	8.5–12.5	Yes	< 4	≈ 11	$\approx 7.2\ \lambda_0$
[32] CPW with ground backing and via	4.7–7.7	Yes	< 4.4	15.1	$\approx 9.8\ \lambda_0$
[33] Double-side parallel strip line	1.2–5.9	Yes	< 5.7	9.7	$\approx 2.9\ \lambda_0$
[34] Dual layer Grounded Dielectric	20.3–26.8	Yes	< 16	16	$12.8\ \lambda_0$
[This Work] SIW	8–12.4	No	< 2	16.1	$12.1\ \lambda_0$

perturbation makes the present antenna appealing for planar circuit integration.

V. CONCLUSION

This paper presents an SIW-based periodic LWA for *X*-band applications. The open stopband at broadside has been suppressed using a series–shunt loaded unit cell. Bloch wave analysis is used to optimize the unit cell dimensions and obtain the antenna propagation characteristics. Q balancing technique is used for broadside gain equalization. The design procedure is detailed with fabrication examples. Two antennas are fabricated to validate the predicted results. The antennas provide a consistent gain over the entire scan range with a gain variation of less than 2 dB over 8–12.4 GHz. The second antenna is designed for reduced SLL. Since the antenna is designed using only a single-layer printed circuit board without any ground plane perturbation, it can be easily integrated into a system. The antenna can be redesigned at any other microwave and lower millimeter-wave bands simply by frequency scaling.

REFERENCES

[1] D. R. Jackson and A. A. Oliner, "Leaky-wave antennas," in *Modern Antenna Handbook*, C. Balanis, Ed. New York, NY, USA: Wiley, 2008.

[2] S. Abielmona, H. V. Nguyen, and C. Caloz, "Analog direction of arrival estimation using an electronically-scanned CRLH leaky-wave antenna," *IEEE Trans. Antennas Propag.*, vol. 59, no. 4, pp. 1408–1412, Apr. 2011.

[3] M. Heddebaut, "Leaky waveguide for train-to-wayside communication-based train control," *IEEE Trans. Veh. Technol.*, vol. 58, no. 3, pp. 1068–1076, Mar. 2009.

[4] S.-T. Yang and H. Ling, "Application of a microstrip leaky wave antenna for range–azimuth tracking of humans," *IEEE Geosci. Remote Sens. Lett.*, vol. 10, no. 6, pp. 1384–1388, Nov. 2013.

[5] M. Ettorre, R. Sauleau, L. Le Coq, and F. Bodereau, "Single-folded leaky-wave antennas for automotive radars at 77 GHz," *IEEE Antennas Wireless Propag. Lett.*, vol. 9, pp. 859–862, 2010.

[6] S. Gupta, S. Abielmona, and C. Caloz, "Microwave analog real-time spectrum analyzer (RTSA) based on the spectral–spatial decomposition property of leaky-wave structures," *IEEE Trans. Microw. Theory Techn.*, vol. 57, no. 12, pp. 2989–2999, Dec. 2009.

[7] A. A. Oliner, "Leakage from higher modes on microstrip line with application to antennas," *Radio Sci.*, vol. 22, pp. 907–912, Nov. 1987.

[8] R. Shaw and M. K. Mandal, "Dual-beam periodic leaky wave antenna with broadside radiation," in *Proc. Asia-Pacific Microw. Conf.*, Dec. 2016, pp. 1–4.

[9] W. Menzel, "A new travelling-wave antenna in microstrip," *Arch. Elek Ubertragung.*, vol. 33, pp. 137–140, Apr. 1979.

[10] L. O. Goldstone and A. A. Oliner, "Leaky-wave antennas I: Rectangular waveguides," *IRE Trans. Antennas Propag.*, vol. 7, pp. 307–319, Oct. 1959.

[11] P. Mondal and K. Wu, "A leaky-wave antenna in substrate integrated non-radiative dielectric (SINRD) waveguide with controllable scanning rate," *IEEE Trans. Antennas Propag.*, vol. 61, no. 4, pp. 2294–2297, Apr. 2013.

[12] A. A. Oliner and P. Lampariello, "Novel leaky-wave antenna for millimetre waves based on groove guide," *Electron. Lett.*, vol. 18, no. 25, pp. 1105–1106, Dec. 1982.

[13] J. Liu, D. R. Jackson, and Y. Long, "Substrate integrated waveguide (SIW) leaky-wave antenna with transverse slots," *IEEE Trans. Antennas Propag.*, vol. 60, no. 1, pp. 20–29, Jan. 2012.

[14] R. Shaw, A. A. Khan, and M. K. Mandal, "Dual-beam substrate integrated waveguide periodic leaky-wave antenna," in *Proc. Int. Conf. Microw. Photon. (ICMAP)*, Dec. 2015, pp. 1–2.

[15] D. Deslandes and K. Wu, "Accurate modeling, wave mechanisms, and design considerations of a substrate integrated waveguide," *IEEE Trans. Microw. Theory Techn.*, vol. 54, no. 6, pp. 2516–2526, Jun. 2006.

[16] W. W. Hansen, "Radiating electromagnetic wave guide," U.S. Patent 2 402 622 A, Oct. 26, 1940.

[17] P. Bonnaval, "Directional slot antenna for very high frequencies," U.S. Patent 3 978 485 A, Aug. 31, 1976.

[18] G. A. Scharp, "Continuous slot antennas," U.S. Patent 4 328 502 A, May 4, 1982.

[19] F. L. Whetten and C. A. Balanis, "Meandering long slot leaky-wave waveguide-antennas," *IEEE Trans. Antennas Propag.*, vol. 39, no. 11, pp. 1553–1560, Nov. 1991.

[20] J. L. Gomez-Tornero, A. T. Martinez, D. C. Rebenaque, M. Gugliemi, and A. Alvarez-Melcon, "Design of tapered leaky-wave antennas in hybrid waveguide-planar technology for millimeter waveband applications," *IEEE Trans. Antennas Propag.*, vol. 53, no. 8, pp. 2563–2577, Aug. 2005.

[21] Y. J. Cheng, W. Hong, K. Wu, and Y. Fan, "Millimeter-wave substrate integrated waveguide long slot leaky-wave antennas and two-dimensional multibeam applications," *IEEE Trans. Antennas Propag.*, vol. 59, no. 1, pp. 40–47, Jan. 2011.

[22] F. Monticone and A. Alù, "Leaky-wave theory, techniques, and applications: From microwaves to visible frequencies," *Proc. IEEE*, vol. 103, no. 5, pp. 793–821, May 2015.

[23] F. Xu, K. Wu, and X. Zhang, "Periodic leaky-wave antenna for millimeter wave applications based on substrate integrated waveguide," *IEEE Trans. Antennas Propag.*, vol. 58, no. 2, pp. 340–347, Feb. 2010.

[24] A. R. Mallahzadeh and M. A. Amini, "Design of a leaky-wave long slot antenna using ridge waveguide," *IET Microw., Antennas Propag.*, vol. 8, no. 10, pp. 714–718, Jul. 2014.

[25] S. Mohammad-Ali-Nezhad and A. Mallahzadeh, "Periodic ridged leaky-wave antenna design based on SIW technology," *IEEE Antennas Wireless Propag. Lett.*, vol. 14, pp. 354–357, Feb. 2015.

[26] L. Liu, C. Caloz, and T. Itoh, "Dominant mode (DM) leaky-wave antenna with backfire-to-endfire scanning capability," *Electron. Lett.*, vol. 38, no. 23, pp. 1414–1416, Nov. 2002.

[27] A. Mallahzadeh and S. Mohammad-Ali-Nezhad, "Periodic collinear-slotted leaky wave antenna with open stopband elimination," *IEEE Trans. Antennas Propag.*, vol. 63, no. 12, pp. 5512–5521, Dec. 2015.

[28] Y. L. Lyu *et al.*, "Leaky-wave antennas based on noncutoff substrate integrated waveguide supporting beam scanning from backward to forward," *IEEE Trans. Antennas Propag.*, vol. 64, no. 6, pp. 2155–2164, Jun. 2016.

[29] Nasimuddin, Z. N. Chen, and X. Qing, "Multilayered composite right/left-handed leaky-wave antenna with consistent gain," *IEEE Trans. Antennas Propag.*, vol. 60, no. 11, pp. 5056–5062, Nov. 2012.
[30] J. S. Gomez-Diaz, A. Alvarez-Melcon, and T. Bertuch, "A modal-based iterative circuit model for the analysis of CRLH leaky-wave antennas comprising periodically loaded PPW," *IEEE Trans. Antenna Propag.*, vol. 59, no. 4, pp. 1101–1112, Apr. 2011.
[31] Y. D. Dong and T. Itoh, "Composite right/left-handed substrate integrated waveguide and half mode substrate integrated waveguide leaky-wave structures," *IEEE Trans. Antennas Propag.*, vol. 59, no. 3, pp. 767–775, Mar. 2011.
[32] A. Mehdipour and G. V. Eleftheriades, "Leaky-wave antennas using negative-refractive-index transmission-line metamaterial supercells," *IEEE Trans. Antennas Propag.*, vol. 62, no. 8, pp. 3929–3942, Aug. 2014.
[33] D. Ye, Y. Li, Z. Liang, J. Liu, S. Zheng, and Y. Long, "Periodic triangle-truncated DSPSL-based antenna with backfire to endfire beam-scanning capacity," *IEEE Trans. Antennas Propag.*, vol. 65, no. 2, pp. 845–849, Feb. 2017.
[34] D. Comite *et al.*, "A dual-layer planar leaky-wave antenna designed for linear scanning through broadside," *IEEE Antennas Wireless Propag. Lett.*, vol. 16, pp. 1106–1110, 2017.
[35] S. Otto, A. Al-Bassam, A. Rennings, K. Solbach, and C. Caloz, "Radiation efficiency of longitudinally symmetric and asymmetric periodic leaky-wave antennas," *IEEE Antennas Wireless Propag. Lett.*, vol. 11, pp. 612–615, 2012.
[36] S. Otto, A. Al-Bassam, A. Rennings, K. Solbach, and C. Caloz, "Transversal asymmetry in periodic leaky-wave antennas for Bloch impedance and radiation efficiency equalization through broadside," *IEEE Trans. Antennas Propag.*, vol. 62, no. 10, pp. 5037–5054, Oct. 2014.
[37] S. Otto, A. Rennings, K. Solbach, and C. Caloz, "Transmission line modeling and asymptotic formulas for periodic leaky-wave antennas scanning through broadside," *IEEE Trans. Antennas Propag.*, vol. 59, no. 10, pp. 3695–3709, Oct. 2011.
[38] R. C. Hansen, *Phased Array Antennas*, 1st ed. New York, NY, USA: Wiley, 1998, ch. 6.
[39] D. M. Pozar, *Microwave Engineering*, 4th ed. Hoboken, NJ, USA: Wiley, 2011.
[40] D. Deslandes, "Design equations for tapered microstrip-to-substrate integrated waveguide transitions," in *IEEE MTT-S Int. Microw. Symp. Dig.*, May 2010, pp. 704–707.
[41] K. Wei, Z. Zhang, Z. Feng, and M. F. Iskander, "Periodic leaky-wave antenna array with horizontally polarized omnidirectional pattern," *IEEE Trans. Antennas Propag.*, vol. 60, no. 7, pp. 3165–3173, Jul. 2012.
[42] J. Liu, D. R. Jackson, Y. Li, C. Zhang, and Y. Long, "Investigations of SIW leaky-wave antenna for endfire-radiation with narrow beam and sidelobe suppression," *IEEE Trans. Antennas Propag.*, vol. 62, no. 9, pp. 4489–4497, Sep. 2014.

Ravi Shaw (S'15) received the B.Tech. degree in electronics and communication engineering from the West Bengal University of Technology, Kolkata, India, in 2008, and the M.Tech. degree in VLSI design from the Indian Institute of Engineering Science and Technology, Shibpur, India, in 2013. He is currently pursuing the Ph.D. degree with the Department of Electronics and Electrical Communication Engineering, IIT Kharagpur, Kharagpur, India.

From 2008 to 2011, he was a Systems Engineer with Infosys Technologies Ltd., Bangalore, India. His current research interests include analysis and design of leaky wave antennas and systems in microwave and millimeter-wave regime.

Mr. Shaw is a Corporate Member of the Institution of Engineers, India. He served as the Chair of the IEEE AP-MTTS Student Branch Chapter, IIT Kharagpur, from 2016 to 2017.

Mrinal Kanti Mandal (S'06–M'08–SM'13) received the B.Sc. degree (Hons.) in physics and the B.Tech. and M.Tech. degrees in radio physics and electronics from the University of Calcutta, Calcutta, India, in 1998, 2001, and 2003, respectively, and the Ph.D. degree from the Department of Electronics and Electrical Communication Engineering, IIT Kharagpur, Kharagpur, India, in 2008.

He was a Research Fellow with the Department of RF and Optical, Institute for Infocom Research, Singapore, from 2007 to 2009. He was a Post-Doctoral Fellow with the University De Québec, Montreal, QC, Canada, from 2009 to 2010, and the Ecole Polytechnique, Montreal, from 2010 to 2012. He is currently an Associate Professor with the Electronics and Electrical Communication Engineering, IIT Kharagpur. He has authored or co-authored over 90 journal and conference papers. His current research interests include design and analysis of microwave and millimeter-wave circuits and systems.